Lawrence Berkeley National Laboratory
Recent Work

Title
Effects of Catalyst Processing on the Activity and Stability of Pt-Ni Nanoframe Electrocatalysts.

Permalink
https://escholarship.org/uc/item/44c45778

Journal
ACS nano, 12(8)

ISSN
1936-0851

Authors
Chen, Shouping
Niu, Zhiqiang
Xie, Chenlu
et al.

Publication Date
2018-08-01

DOI
10.1021/acsnano.8b04674

Peer reviewed

Effects of Catalyst Processing on the Activity and Stability of Pt−Ni Nanoframe Electrocatalysts

Shouping Chen,[†,§,⊥] Zhiqiang Niu,[‡,⊥] Chenlu Xie,[‡] Mengyu Gao,[†,§] Minliang Lai,[‡] Mufan Li,[§] and Peidong Yang*[,†,§,‡,∥]

[†]Department of Materials Science and Engineering and [‡]Department of Chemistry, University of California, Berkeley, California 94720, United States

[§]Materials Science Division, Lawrence Berkeley National Laboratory, Berkeley, California 94720, United States

[∥]Kavli Energy NanoSciences Institute, Berkeley, California 94720, United States

S *Supporting Information*

ABSTRACT: Pt-based alloys have shown great promise as cathodic catalysts for cost-effective proton-exchange membrane fuel cells. Post-synthesis treatment has been recognized as a critical step to improve the catalytic performance of Pt-based alloys. Here, we present the effects of catalyst processing on the catalytic behavior of Pt−Ni nanoframe electrocatalysts in oxygen reduction reaction. The Pt−Ni nanoframes were made by corroding the Ni-rich phase from solid rhombic dodecahedral particles. A total of three different corrosion procedures were compared. Among them, electrochemical corrosion led to the highest initial specific activity (1.35 mA cm^{-2} at 0.95 V *versus* reversible hydrogen electrode) by retaining more Ni in the nanoframes. However, the high activity gradually went down in a subsequent stability test due to continuous Ni loss and concomitant surface reconstruction. On the other hand, the best stability was achieved by a more-aggressive corrosion using oxidative nitric acid. Although the initial activity was compromised, this procedure imparted a less-defective surface, and thus, the specific activity dropped by only 7% over 30 000 potential cycles. These results indicate a delicate trade-off between the activity and stability of Pt−Ni nanoframe electrocatalysts. The obtained understanding of how to balance the activity−stability trade-off *via* catalyst processing can be generalized to other Pt-based alloys.

KEYWORDS: oxygen reduction reaction, platinum−nickel electrocatalyst, post-synthesis treatment, degradation trajectory, nanoframe
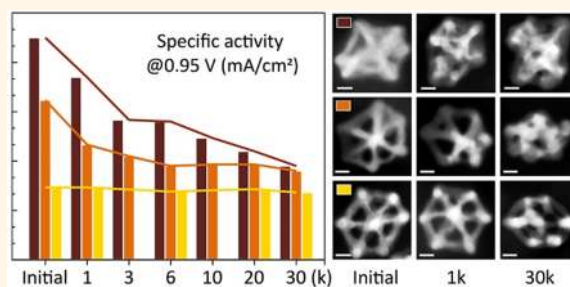
The proton-exchange membrane fuel cells (PEMFCs) powered by hydrogen from renewable sources serve as the most-promising power supplies for future transportation applications.[1] However, the high cost of Pt, which exhibits the highest activity for the overall efficiency-limiting cathodic oxygen reduction reaction (ORR),[2] is the major limitation preventing the large-scale deployment of PEMFCs in automotive vehicles.[3] To achieve commercially viable PEMFCs, highly durable cathodic catalysts with low Pt loading are required. Pt-based alloys have been discovered to hold the promise to affordable PEMFCs due to their outstanding ORR activity.[4] Alloying Pt with a proper transition metal results in a downshift of the d-band center, which, in turn, weakens the Pt−OH$_{ad}$ bonding and increases the ORR rate.[5,6] Different strategies, including size, shape, and composition control,[7,8] have been frequently used to optimize the activity and durability of Pt-based alloy catalysts.[9−11] The development of Pt−Ni octahedral nanoparticles is a representative example. As

a nanoscale replica of the ideal (111) single-crystalline surface,[12] the Pt$_3$Ni octahedra are enclosed by high-coordination surface atoms that are favorable for the desorption of oxygenated species. Therefore, the Pt−Ni octahedra exhibit much-higher specific activity than the spherical analogues.[13,14]

Although the controlled synthesis plays an important role in the development of advanced ORR catalysts, post-synthesis treatment has been shown to be of equal importance in the tailoring of their catalytic behavior.[15−18] The near-surface structure and composition of freshly made nanostructures can change upon exposure to air, moisture, heat, corrosive solvent, acid, and other unidentified environment factors. In particular,

heat treatment is commonly adopted as a necessary step not only to form better contacts between catalytic particles and carbon support but also to induce the desired surface relaxation and reconstruction.[19−23] Studies have shown that carefully choosing the annealing temperature and atmosphere can generate an enhanced degree of alloying as well as an optimal extent of Pt surface enrichment. These structural changes have brought great benefits to both the ORR reactivity and durability.[21] Another widely used post-synthesis treatment is the pre-leaching of transition metals.[24−26] The electro-chemical dissolution of transition metals during fuel cell operation can cause detrimental contamination to the membrane and ionomer.[18] Acid washing is therefore a necessity before the Pt-based alloy catalysts can be used in PEMFCs. Because the leaching of transition metals always starts from the topmost layers, a Pt-rich shell is concomitantly generated and, in turn, acts as a protective layer to prevent further acid corrosion of the transition metals. The as-obtained core−shell structures preserve a composition gradience and constitute one type of the most-active and -stable ORR catalysts.[26]

Our group recently developed the Pt−Ni nanoframe electrocatalysts by manipulating the spatial positioning of Pt and Ni in the solid rhombic dodecahedra (RD).[27−29] The elegant control over the morphology at nanoscale together with the formation of a smooth Pt-skin surface at atomic scale lead to exceptional ORR performance. The nanoframes were realized by removing the Ni-rich phase from the parent Pt−Ni RD through either ambient oxidation[27] or acetic acid treatment.[28,29] In the practice of ORR measurement, however, we noticed that the corrosion procedure had non-negligible influences on the catalytic performance. The ORR activity and durability of Pt−Ni nanoframes fluctuated in a wide range depending on how they were processed. In this regard, we here systematically compared three different corrosion procedures to provide a better understanding of how catalyst processing affects the composition and surface structure of Pt−Ni nanoframes and, thus, their catalytic activity and stability.

RESULTS AND DISCUSSION

To compare the effects of catalyst processing, we first synthesized Pt−Ni RD by the hot injection of metal precursors in oleylamine at 265 °C (for more details, see the Methods section). The Pt−Ni RD were then subjected to different processing procedures, as shown in Scheme 1. In the first procedure, the as-synthesized Pt−Ni RD were directly loaded on carbon without removing the Ni-rich phase. We anticipated that excessive Ni in the solid RD would be eliminated by subsequent electrochemical corrosion. In the second and third procedures, the solid Pt−Ni RD were corroded before loading by a mild organic acid (acetic acid) and a strong oxidative acid (nitric acid), respectively. The acetic acid corrosion, a standard method to make nanoframes in our previous work,[28,29] was employed here as a benchmark. The nitric acid is certainly more aggressive than acetic acid, and a higher degree of chemical corrosion was therefore expected. After being loaded on carbon, the catalysts were annealed in air at 180 °C to remove the organic ligands. The air-annealed catalysts were stored in N_2 box with a dehumidification system at ambient temperature to exclude the influence of other environment factors.

Before the evaluation of the electrocatalytic performance, the catalysts were pretreated or "activated" by potential cycling in

Scheme 1. Flow Chart of Three Processing Procedures Applied to the As-Synthesized Pt−Ni Rhombic Dodecahedra, Termed as" proc. 1", "proc. 2", and "proc. 3", Respectively[a]
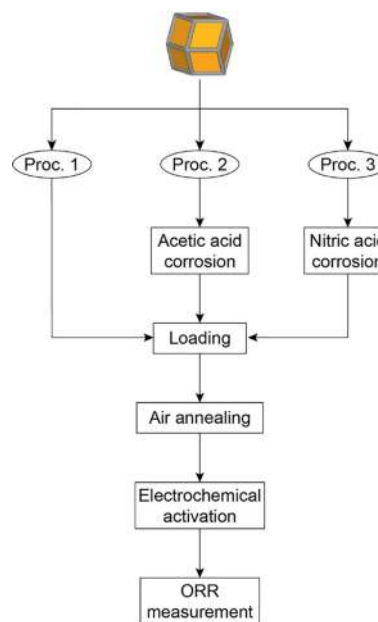
[a]In the geometrical model of rhombic dodecahedra, the gray color represents the Pt-rich phase, and the orange color represents the Ni-rich phase.

Ar-saturated $HClO_4$ solution between 0.05 and 1.02 V versus reversible hydrogen electrode (V_{RHE}) with a sweep rate of 100 mV s^{-1} in a three-electrode rotating disc electrode setup (Scheme 1, electrochemical activation). This process was monitored by tracking the changes of cyclic voltammetric profiles until both the hydrogen and the hydroxyl adsorption−desorption regions became stable. Figure S1 shows the cyclic voltammograms (CVs) of the three samples at representative cycles. For the catalyst processed by procedure 1, the CVs kept enlarging significantly in the first 80 cycles (Figure S1a). This dramatic profile change can be explained by the massive Ni dissolution from the Ni-rich Pt−Ni RD driven by the potential cycling.[30] The expansion of the CV profiles is an indicator of the gradual exposure of Pt after the Ni dissolution. Electro-chemical activation was also applied to the catalyst processed by procedure 2. The CVs exhibited a smaller expansion than that of procedure 1 and held steady after 50 cycles (Figure S1b). It suggests that there was still a small amount of unalloyed Ni species remained at outermost layers after acetic acid corrosion, which leached out during the electrochemical activation. For the catalyst processed by procedure 3, on the contrary, the CV variation was almost negligible from the very first cycle to the 35th cycle (Figure S1c). The barely changed CV profiles suggest that nitric acid corrosion was very effective to get rid of the excessive near-surface Ni and resulted in a fairly stable surface. The above explanations for the CV changes are mainly connected to the Ni dissolution, which were later validated by tracking the composition evolutions using energy-dispersive X-ray spectroscopy (EDX).

After the electrochemical activation, the ORR activity and stability of the three catalysts were evaluated (Scheme 1, ORR measurement). Figure 1a−c shows the CV curves of each catalyst right after activation as well as after 1000 and 30 000
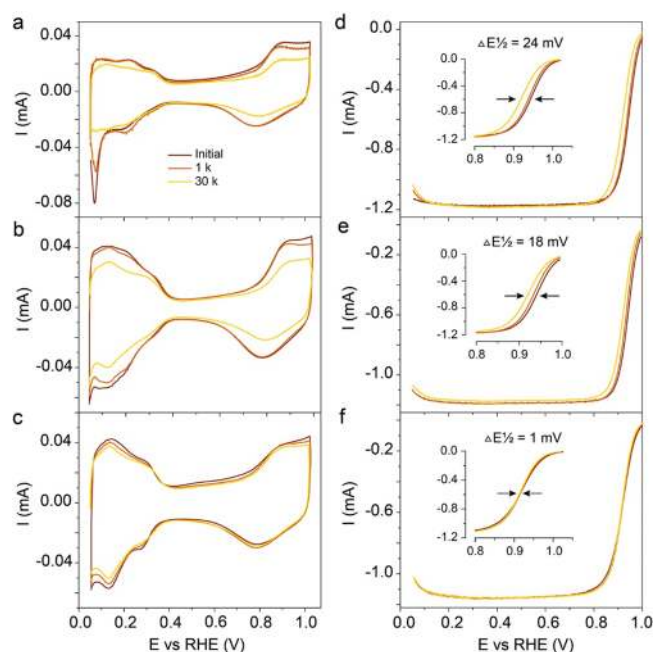
Figure 1. (a−c) Cyclic voltammograms and (d−f) ORR polarization curves of the catalysts processed by procedures (a, d) 1, (b, e) 2, and (c, f) 3. The initial measurement as well as after 1000 and 30 000 ADT cycles were plotted for comparison. Cyclic voltammogram was measured in Ar-saturated 0.1 M $HClO_4$ electrolyte with a sweep rate of 50 mV s^{-1}. ORR activity was measured in O_2-saturated 0.1 M $HClO_4$ electrolyte with a sweep rate of 20 mV s^{-1} and a rotation rate of 1600 rpm. ADT was conducted in Ar-saturated 0.1 M $HClO_4$ electrolyte between 0.50 and 1.00 V_{RHE} with a sweep rate of 200 mV s^{-1}.

cycles of accelerated durability testing (ADT). The electrochemically active surface areas (ECSAs) of each catalyst were calculated using the charges associated with hydrogen underpotential deposition (H_{upd}) normalized to the Pt mass loading. As shown in Figure 2a, the initial ECSAs for the three catalysts were 40.1 m^2 g$_{Pt}^{-1}$ (procedure 1), 56.6 m^{2}g$_{Pt}^{-1}$ (procedure 2), and 54.8 m^2 g$_{Pt}^{-1}$ (procedure 3), respectively. The catalysts obtained by acetic acid corrosion and nitric acid corrosion had similar surface areas that were consistent with the previously reported values for Pt−Ni nanoframes.[28,29] The electrochemical corrosion of Pt−Ni RD (procedure 1), however, resulted in a surprisingly low ECSA compared with the other two processes. Given that a substantial Ni dissolution occurred during the electrochemical activation step, we attributed the low ECSA as a consequence of surface reconstruction associated with the massive Ni loss. This interpretation was later supported by the catalyst morphology changes revealed by transmission electron microscopy (TEM). It should be mentioned that the ratios of CO_{ad} to H_{upd} for all the three catalysts are close to 1.0, where CO_{ad} represents the ECSA calculated from the CO-stripping.[31] The degradation trajectories of the ECSAs were also plotted in Figure 2a. In general, all the three catalysts underwent gradual decreases along with the potential cycles. The ECSAs after 30 000 ADT cycles were 34.5 m^2 g$_{Pt}^{-1}$ (procedure 1), 41.2 m^2 g$_{Pt}^{-1}$ (procedure 2), and 47.2 m^2 g$_{Pt}^{-1}$ (procedure 3), respectively. The catalyst treated by nitric acid corrosion had much less ECSA loss (14%) than that by acetic acid corrosion (27%), although their initial ECSAs were at the same level. Consistent with what has been learned from the earlier comparison of CV
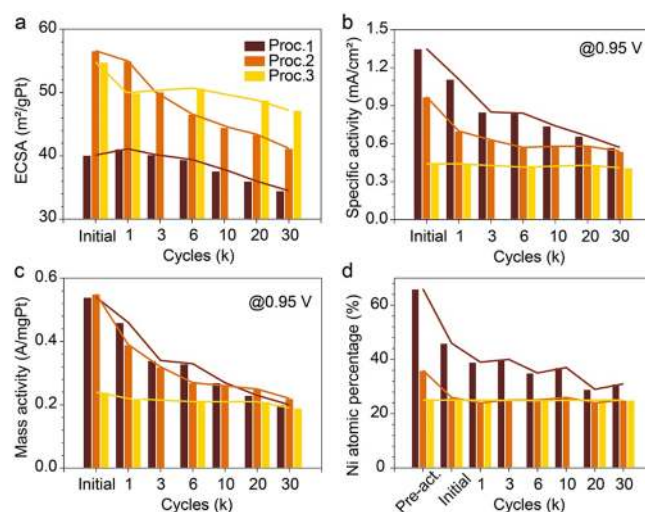

Figure 2. (a) Electrochemically active surface area, (b) specific activity at 0.95 V_{RHE}, (c) mass activity at 0.95 V_{RHE}, and (d) Ni atomic percentage of the catalysts processed by procedures 1, 2, and 3 at representative stages. Here, "pre-act." represents the stage before the electrochemical activation, "initial" represents the initial ORR measurement after the activation, and numbers represent the stages after different ADT cycles, respectively.

variations during the electrochemical activation, these results also suggest that a more-robust surface was delivered by nitric acid corrosion.

The ORR polarization curves of the three catalysts are compared in Figure 1d−f. The amplitudes of negative shift show a direct visual evidence of the decreases in ORR activity following the order of procedure 1 > procedure 2 > procedure 3. The half-potential change after 30 000 cycles is 24 mV for procedure 1, 18 mV for procedure 2, and only 1 mV for procedure 3, respectively. The calculated kinetic currents at 0.95 V_{RHE} from the ORR polarization curves were normalized to the surface areas and Pt mass loadings to give the specific and mass activities, respectively. The results were summarized in Figure 2b,c. Remarkably, the catalyst processed by electrochemical corrosion (procedure 1) exhibited an initial specific activity as high as 1.35 mA cm^{-2} (Figure 2b), almost an order of magnitude higher than that for commercial Pt/C (0.14 mA cm^{-2}). Considering that the specific activities of the hollow Pt−Ni nanoframes made in our lab were exclusively in the range of 0.5−1.0 mA cm^{-2}, the easily reproducible 1.35 mA cm^{-2} obtained by procedure 1 is quite unusual. The origins of this unusual specific activity and the aforementioned low ECSA were discussed later. For the catalyst treated by acetic acid (procedure 2), the initial specific activity was 0.97 mA cm^{-2} (Figure 2b), at a similar level to that in our previous report.[28] The initial specific activity for the catalyst corroded by nitric acid (procedure 3) was 0.44 mA cm^{-2} (Figure 2b), about one-third that of procedure 1. Despite the low initial activity, procedure 3 stands out when taking the durability into consideration. Only 7% specific activity loss was observed after 30 000 ADT cycles (Figure 2b). This long-term stability agrees with the above-discussed ECSA data and electrochemical activation CVs. In a sharp contrast, the highest specific activity obtained by procedure 1 suffered a steep decline and ended up with 58% loss (Figure 2b). This observation suggests that the highly reactive surface sites generated by electrochemical dealloying are vulnerable under long-term fuel cell operation.
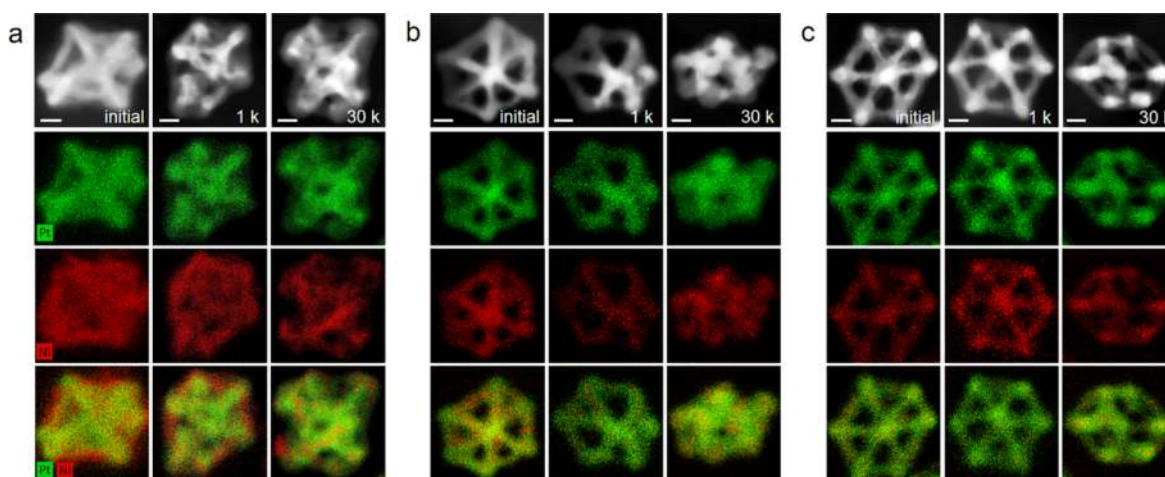
Figure 3. HAADF-STEM and EDX mapping images of the catalysts processed by procedures (a) 1, (b) 2, and (c) 3 after the initial ORR measurement as well as after 1000 and 30 000 ADT cycles. In the EDX maps, green color represents Pt and red color represents Ni, respectively. Scale bar is 5 nm in all images.

Different from both procedures 1 and 3, the degradation of the catalyst processed by procedure 2 featured a fast decrease before 3000 cycles and thereafter reached a plateau (Figure 2b). Figure 2c charts the initial mass activities of the three catalysts and their deactivations. The initial mass activities for the catalysts of procedures 1 and 2 were both around 0.55 A mg_{Pt}^{-1}, while it was 0.24 A mg_{Pt}^{-1} for the catalyst of procedure 3. Notably, though the beginning-of-life mass activities were different, the end-of-life mass activities of the three catalysts all converged to 0.2 A mg_{Pt}^{-1}.

To elucidate the origins of the different catalytic behavior, catalysts after the ORR test were characterized in terms of composition, elemental distribution, morphology, and atom arrangement. Because the Ni composition in the near-surface region plays a key role in improving the ORR activity by weakening the binding of oxygenate species to Pt,[5,6,13,24] we first investigated the variations of Ni atomic percentage (quantified by EDX spectra) in Pt−Ni nanoframe catalysts through their entire lifetime. For the catalyst processed by procedure 1, the Ni atomic percentage before the electrochemical activation was as high as 66%. Such a high Ni content is reasonable because no pre-leaching treatment was performed in procedure 1, and the composition of $Pt_{34}Ni_{66}$ agrees well with the solid Pt−Ni RD.[28] There was a rapid drop from 66% to 46% after the initial ORR measurement, suggesting a substantial Ni loss. This observation is consistent to the large expansion of CVs during the electrochemical activation step (Figure S1a). The decrease of the Ni composition slowed down after the initial ORR measurement. It gradually fell to 31% after 30 000 cycles of ADT. For the catalyst processed by procedure 2, the Ni composition was 36% before the electrochemical activation, decreased to 26% after the initial ORR measurement, and held steady thereafter. The initial decrease of the Ni content is also reflected by the evolution of CVs during the electrochemical activation (Figure S1b). It is worth noting that the dissolution of Ni stopped at a stable Pt_3Ni composition. Lastly, the catalyst treated by procedure 3 already reached a stable Pt_3Ni composition after nitric acid corrosion and stayed the same throughout the whole lifetime, which was, again, in good agreement with the results shown in Figure S1c.

Several implications can be drawn from the above composition study. First, the high initial Ni atomic percentage is very likely to be a major contributor to the unusual high specific activity for the catalyst processed by procedure 1. Second, the Ni depletion seems to be unstoppable before reaching the stable Pt_3Ni composition. Third, pre-leaching can provide additional handles with which to balance the initial ORR activity and long-term stability by changing the starting Ni content in the catalysts. Although the mass activities after 30 000 cycles were very close for all the three procedures, we think that procedure 3 is a more-appropriate practice for the future catalyst processing because it provides more-stable performance in the long run. Meanwhile, the minimum electrochemical dissolution of Ni in procedure 3 (Figure 2d) will not impair the performance of the ionomer and membrane in PEMFCs.[18]

However, comparing the composition evolutions of procedures 2 and 3 (Figure 2d), we noticed that the specific activities of procedure 2 were always higher than those of procedure 3 despite the same Ni atomic percentage. This independence implies that the near-surface compositions were different in these two cases. Further characterizing the spatial distribution of Ni within a single particle is therefore needed. Figure 3 shows the high-angle annular dark-field scanning transmission electron microscopy (HAADF-STEM) and the STEM−EDX mapping images of the catalysts at representative ADT cycles. The elemental maps of the catalysts after the initial ORR measurement clearly showed the surface enrichment of Ni in a descending order of procedure 1 ≫ procedure 2 > procedure 3. The more the Ni enriches in the near-surface region, the higher the ORR activity is. A thin Ni layer was still visible even after 1000 cycles for procedure 1 (Figure 3a); it is no wonder that the high specific activity retained (up to 1.1 mA cm^{-2}). Although it is hard to tell the difference between procedures 2 and 3 after 1000 cycles, more Ni surface enrichment can be confirmed for procedure 2 after 30 000 cycles. Moreover, the particle morphologies are outlined by the HAADF-STEM images. Interestingly, while the catalysts treated by procedures 2 and 3 presented the typical hollow structures after the initial ORR test, the one by procedure 1 appeared to be more solid and more ill-defined (Figure 3a). Moreover, for procedure 2, the well-defined nanoframe was
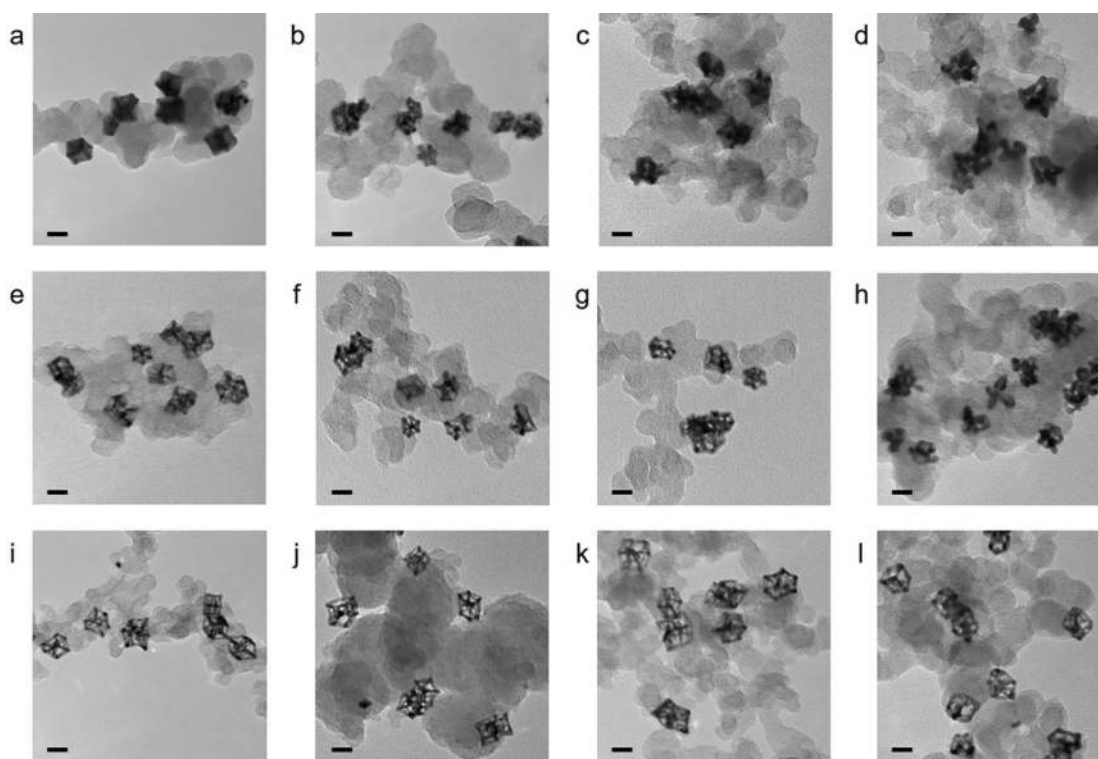
Figure 4. Low-magnification TEM images of the catalysts processed by procedures (a−d) 1, (e−h) 2, and (i−l) 3 (a, e, i) before the electrochemical activation, (b, f, j) after the initial ORR measurement, and after (c, g, k) 1000 and (d, h, l) 30 000 ADT cycles. Scale bar is 20 nm in all images.

destroyed along with the stability test and became difficult to recognize after 30 000 cycles (Figure 3b), whereas the morphology was preserved all along for procedure 3 (Figure 3c).

The morphology evolutions of the catalysts were further investigated by TEM at low magnifications to picture the ensembles of the particles (Figures 4 and S2). Certainly, the low-magnification TEM images provide strong support to the above conclusions. The electrochemical corrosion of the solid RD (Figure 4a) led to partly corroded particles (Figure 4b) rather than nanoframes. The semihollow morphology has an intrinsically small surface-area-to-volume ratio, rationalizing the observed low ECSA. These particles had hexagonal projections on the carbon support after the initial ORR measurement (Figure 4b). The contours of the particles became rough after 1000 cycles (Figure 4c) and evolved to irregular shape after 30 000 cycles (Figure 4d). This morphology evolution is associated with the dissolution of Ni during the electrochemical measurement. As mentioned earlier, a 20% Ni loss occurred (from 66% to 46%) after the initial ORR measurement. Such a large amount of Ni dissolution could generate lots of surface vacancies and even porosities, leaving a so-called Pt-skeleton surface.[17,22,32] Given that defects can enhance the mobility and dissolution of Pt,[7,33,34] a succession of surface reconstruction is expected, eventually leading to the morphology change and ECSA loss. Under the same framework, the deconstruction of the nanoframe observed in procedure 2 (Figure 4e−h) could be governed by a similar dissolution−diffusion−reconstruction process. Figure 4i−l describes the morphology evolution of the catalyst pre-corroded by nitric acid (procedure 3). In addition to the well-maintained nanoframe configuration, the sharp corners of the frame gradually turned rounded, especially after

30 000 cycles of ADT. This observation supports the notion that the under-coordinated surface atoms are more susceptible to surface diffusion and/or electrochemical dissolution.[35,36] These results collectively substantiated that the stable Pt₃Ni composition achieved by a pre-corrosion using nitric acid could prevent the undesired electrochemical Ni dissolution that triggered a series of adverse effects in the other two procedures.

In an attempt to verify the existence of surface defects generated by the electrochemical Ni dissolution, the atom arrangements of the catalysts were studied by high-resolution TEM (HRTEM). Figure S3 shows the HRTEM images and the fast Fourier transforms (FFTs) of the catalysts after the initial ORR measurement. All three particles were highly crystalline with face-centered cubic (fcc) structures. An obvious morphological difference was confirmed by comparing the particles of procedure 1 (Figure S3a) and procedure 3 (Figure S3c), both oriented to the <110> zone axis. Unfortunately, when focusing on the surface of each particle, we could hardly resolve the atom arrangement in accuracy due to the presence of ghost atoms.

We then turned our attention to the potential effects of the mild air annealing because thermal treatments were believed to be able to modify particle structures.[15,17,19−23] Overnight air annealing at 180 °C was applied to all the three catalysts for the purpose of surface cleaning (Scheme 1). Powder X-ray diffraction (XRD) was performed to study the catalyst structural changes during this process. As shown in Figure S4a, the as-synthesized Pt−Ni RD exhibited asymmetric peaks, resulting from the coexistence of the Pt-rich and Ni-rich phases in the solid particles.[28] Catalyst loading did not alter the XRD patterns in terms of shape, position, and width (Figure S4b). After the air annealing, however, all the reflections shifted

Scheme 2. Schematic Diagram of the Atomic Structures of the Catalysts at Representative Stages in Procedures 1, 2, and 3, Respectively[a]
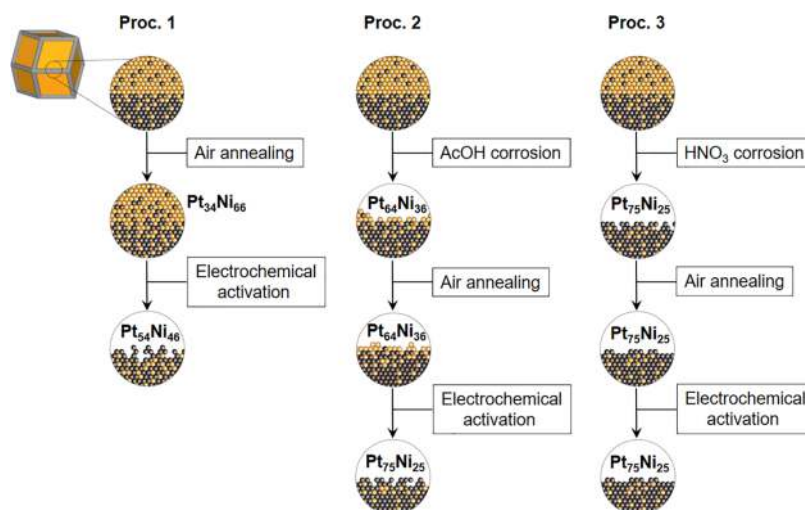
[a]The Pt-rich—Ni-rich interface in the solid rhombic dodecahedron was highlighted by a circle and depicted in detail. The orange color represents Ni, and the gray color represents Pt, respectively. The acid corrosion and air annealing are two key factors determining the remaining Ni content and surface roughness after the electrochemical activation.

toward smaller Bragg angles and the peak profiles became more symmetric in procedure 1 (Figure S4c). These changes indicate an increased alloying extent through thermally driven atomic diffusion at the Pt-rich—Ni-rich interface. The increased alloying extent is in good agreement with the high Ni content remained after the electrochemical activation in procedure 1. Meanwhile, the full width at half-maximum (FWHM) of the XRD profiles had no obvious change, suggesting the grain sizes were well maintained during this low-temperature treatment. The evolutions of the XRD patterns of the catalysts processed by procedure 2 (Figure S4d—f) and procedure 3 (Figure S4g—i) were also followed. Different to what was observed for procedure 1, the XRD profiles of the two catalysts before air annealing were in perfect Gaussian shapes, corresponding to the single-alloy phase. Not surprisingly, there was little change in the XRD patterns after air annealing. Because most Ni had been chemically corroded in advance, atomic interdiffusion lost necessary conditions. Moreover, the (111) reflections of the annealed catalysts (Figure S4c,f,i) had a progressive shift toward lower two theta values, reflecting the decreased Ni content in the order of procedure 1 > procedure 2 > procedure 3. While the XRD provides structural information on Ni in the bulk, our previous X-ray absorption spectroscopy (XAS) study has shown that surface Ni can be oxidized during air annealing and then removed during electrochemical measurement.[31]

With the thorough investigations of the degradation trajectories and the characterizations of the catalysts at representative stages, our hypothesis could be depicted as Scheme 2. Among all the post-synthesis treatment procedures, we believe the acid corrosion and air annealing are the two key steps that regulate the delicate balance between the ORR activity and durability of Pt—Ni nanoframe catalysts. The acid corrosion was utilized to remove the Ni-rich phase in the solid Pt—Ni RD and, thus, to alter the Ni atomic percentage in the final Pt—Ni nanoframes (procedures 2 and 3). The air annealing was employed to remove the organic ligands (procedures 1–3), yet was also able to enhance the alloying extent via atomic interdiffusion (procedure 1). The combina-

tion of the two factors not only defines the starting Ni composition (and, thus, the initial activity) but also determines the magnitude of Ni dissolution during the electrochemical measurement (and, thus, the durability). We believe the magnitude of Ni dissolution is related to the formation of low-coordinated surface sites, which is a major trigger for the destruction of the surface structure and the particle morphology (and, hence, the decrease of ECSA, specific activity, and mass activity). Finding ways to annihilate the electrochemical Ni dissolution holds the key to less-defective surfaces and will be the focus of our future work.

CONCLUSIONS

In conclusion, we have developed three different catalyst processing procedures to understand the effects of post-synthesis treatment on the ORR performance of Pt—Ni nanoframe electrocatalysts. We systematically varied the chemical corrosion extents of the Pt—Ni RD before loading (namely, noncorrosion, mild corrosion, and strong corrosion). The initial ORR activities as well as the degradation trajectories of ECSA, specific activity, and mass activity were compared. The results indicate a compromise between the activity and stability of Pt—Ni nanoframes. By characterizing the evolutions of the bulk composition, elemental distribution, and morphology using TEM, HAADF-STEM, EDX, HRTEM, and XRD, we have correlated the resulting ORR activity and stability to the Ni content in the catalysts. While the initial Ni contents are the major contributors to the different ORR activities, the electrochemical Ni dissolution triggers a cascade of structural changes that account for the catalyst deactivation. These results could serve as a guideline on how to accomplish desired properties by catalyst processing for a variety of bimetallic electrocatalysts.

METHODS

Chemicals. Chloroplatinic acid hexahydrate (H$_2$PtCl$_6$·6H$_2$O, ≥ 37.5% Pt basis), nickel(II) nitrate hexahydrate (Ni(NO$_3$)$_2$·6H$_2$O, ≥ 98.5%), oleylamine (technical grade, 70%), and hexane (≥98.5%) were purchased from Sigma-Aldrich. Toluene (≥99.9%) was

purchased from Fisher Scientific. Acetic acid (≥99.7%) was purchased from EMD. Nitric acid (≥69.0%) and perchloric acid (67−72%) were purchased from Honeywell Fluka. Carbon black (Vulcan XC-72) was purchased from Cabot Corporation. Commercial Pt, nominally 20 wt % on carbon black, was purchased from Alfa Aesar.

Characterizations. Transmission electron microscopy and quantitative energy dispersive X-ray spectroscopy were carried out using Hitachi H-7650 equipped with EDAX microanalysis. High-resolution TEM was acquired by FEI Tecnai F20 at an accelerating voltage of 200 kV. High-angle annular dark-field scanning transmission electron microscopy and EDX mapping were performed with FEI TitanX 60−300. Inductively coupled plasma optical emission spectroscopy (ICP-OES) was tested using PerkinElmer Optima 7000 DV. X-ray diffraction was measured by a Bruker D-8 General Area Detector Diffraction System (GADDS) with Co Kα source.

Synthesis of Pt−Ni Rhombic Dodecahedra. In a typical synthesis, 20 mg of $H_2PtCl_6 \cdot 6H_2O$ and 14.5 mg of $Ni(NO_3)_2 \cdot 6H_2O$ were dissolved in 0.7 mL of oleylamine in a small centrifuge tube. The precursor solution was injected into a three-necked flask charged with oleylamine (9 mL) that had been preheated at 160 °C for 1 h under nitrogen (N_2) purging. After the injection, the reaction was kept under vacuum for 2.5 min. Next, the reaction was heated to 265 °C with a ramping rate of 15 °C min^{-1} under N_2. The color of the solution changed from green to yellow, brown, and, finally, black after the temperature reached 265 °C. The reaction was stopped at 4 min after the solution turned black by carefully transferring the flask into a water bath to quench the growth. The products were washed twice with a hexane/ethanol mixture and collected by centrifugation at 12 000 rpm.

Acetic Acid Corrosion. The Pt−Ni rhombic dodecahedra collected by centrifugation were redispersed in 2 mL of toluene by brief sonication and then mixed with 5 mL of acetic acid. The mixture was heated at 90 °C under vigorous stirring for 2 h in air to allow the evolution from Pt−Ni rhombic dodecahedra to Pt−Ni nanoframes. The products were washed twice with a hexane/ethanol mixture and collected by centrifugation at 12 000 rpm.

Nitric Acid Corrosion. The Pt−Ni rhombic dodecahedra collected by centrifugation were redispersed in 10 mL of nitric acid (2M) aqueous solution by intense sonication. The mixture was heated at 70 °C under vigorous stirring for 12 h in air to corrode Pt−Ni rhombic dodecahedra into Pt_3Ni nanoframes. The products were first washed once with pure ethanol and then washed twice with a hexane/ethanol mixture. After each wash, the sample was collected by centrifugation at 12 000 rpm.

Electrochemical Measurements. The as-synthesized or acid-corroded Pt−Ni rhombic dodecahedra were redispersed in chloroform and added to carbon in a ratio that produced a loading of 18−20 wt % Pt. The mixture was shaken or sonicated in chloroform for 3 to 5 min to complete the loading process. The loaded catalyst was washed twice with hexane and collected by centrifugation at 10 000 rpm. The resulting black powder was heated at 180 °C in air for 14 h to remove the organic ligands. The carbon supported catalyst was then dispersed in water with a concentration of 0.5 $mg_{catalyst}$ mL^{-1}. The actual concentration of Pt in the ink was determined by ICP-OES. The catalyst ink was deposited onto a glassy carbon rotating disk electrode (Pine Instruments, 0.196 cm^2) in the appropriate volume to achieve about 10 μg_{Pt} cm^{-2} loading density. The commercial Pt/C catalyst had a loading density of 7.8 μg_{Pt} cm^{-2}. The electrochemical measurements were conducted in a three-compartment glass electrochemical cell with a Pine rotating disk electrode (RDE) setup and a Biologic VSP potentiostat. A saturated Ag/AgCl electrode and a Pt wire were used as reference and counter electrodes, respectively, and 0.1 M $HClO_4$ prepared from 67% $HClO_4$ was used as the electrolyte. All potentials are presented *versus* the RHE. The catalyst was typically held at 0.05 V *versus* RHE between measurements, and the limits of the cyclic voltammetry were 0.05−1.02 V. Hydrogen underpotential deposition measurements were performed by saturating the electrolyte with argon gas before collecting the CV at a sweep rate of 50 mV s^{-1}. The ORR activity measurements were carried out under oxygen (O_2)-purging

conditions and at a sweep rate of 20 mV s^{-1} with an RDE rotation rate of 1600 rpm. The accelerated durability testing (ADT) was conducted by potential cycling in Ar-saturated 0.1 M $HClO_4$ electrolyte between 0.60 and 1.00 V with a sweep rate of 200 mV s^{-1} for different number of cycles. The currents for ORR were corrected for an ohmic potential drop (*iR* drop). All of the electrochemical measurements were conducted at room temperature.

ASSOCIATED CONTENT

Ⓢ Supporting Information

The Supporting Information is available free of charge on the ACS Publications website at DOI: 10.1021/acsnano.8b04674.

> Experimental details and additional characterization data. Figures showing cyclic voltammograms, lower-magnification TEM images, HRTEM images, and XRD patterns. (PDF)

AUTHOR INFORMATION

Corresponding Author
*E-mail: p_yang@berkeley.edu.

ORCID Ⓞ
Shouping Chen: 0000-0002-5223-6336
Zhiqiang Niu: 0000-0002-9122-4880
Chenlu Xie: 0000-0001-9215-6878
Peidong Yang: 0000-0003-4799-1684

Author Contributions
⊥S.C. and Z.N. contributed equally.

Notes
The authors declare no competing financial interest.

REFERENCES

(1) Debe, M. K. Electrocatalyst Approaches and Challenges for Automotive Fuel Cells. *Nature* **2012**, *486*, 43−51.

(2) Nørskov, J. K.; Rossmeisl, J.; Logadottir, A.; Lindqvist, L.; Kitchin, J. R.; Bligaard, T.; Jonsson, H. Origin of the Overpotential for Oxygen Reduction at a Fuel-Cell Cathode. *J. Phys. Chem. B* **2004**, *108*, 17886−17892.

(3) Gasteiger, H. A.; Marković, N. M. Just a Dream-or Future Reality? *Science* **2009**, *324*, 48−49.

(4) Stamenkovic, V. R.; Mun, B. S.; Arenz, M.; Mayrhofer, K. J.; Lucas, C. A.; Wang, G.; Ross, P. N.; Markovic, N. M. Trends in Electrocatalysis on Extended and Nanoscale Pt-Bimetallic Alloy Surfaces. *Nat. Mater.* **2007**, *6*, 241−247.

(5) Stamenkovic, V.; Mun, B. S.; Mayrhofer, K. J.; Ross, P. N.; Markovic, N. M.; Rossmeisl, J.; Greeley, J.; Nørskov, J. K. Changing the Activity of Electrocatalysts for Oxygen Reduction by Tuning the Surface Electronic Structure. *Angew. Chem., Int. Ed.* **2006**, *45*, 2897−2901.

(6) Stamenkovic, V. R.; Mun, B. S.; Mayrhofer, K. J.; Ross, P. N.; Markovic, N. M. Effect of Surface Composition on Electronic Structure, Stability, and Electrocatalytic Properties of Pt-Transition Metal Alloys: Pt-Skin *versus* Pt-Skeleton Surfaces. *J. Am. Chem. Soc.* **2006**, *128*, 8813−8819.

(7) Shao, M.; Chang, Q.; Dodelet, J.-P.; Chenitz, R. Recent Advances in Electrocatalysts for Oxygen Reduction Reaction. *Chem. Rev.* **2016**, *116*, 3594−3657.

(8) Wang, Y.-J.; Zhao, N.; Fang, B.; Li, H.; Bi, X. T.; Wang, H. Carbon-Supported Pt-Based Alloy Electrocatalysts for the Oxygen Reduction Reaction in Polymer Electrolyte Membrane Fuel Cells: Particle Size, Shape, and Composition Manipulation and Their Impact to Activity. *Chem. Rev.* **2015**, *115*, 3433−3467.

(9) Zhang, L.; Roling, L. T.; Wang, X.; Vara, M.; Chi, M.; Liu, J.; Choi, S.-I.; Park, J.; Herron, J. A.; Xie, Z.; Mavrikakis, M.; Xia, Y. Platinum-Based Nanocages with Subnanometer-Thick Walls and Well-Defined, Controllable Facets. *Science* **2015**, *349*, 412−416.

(10) Li, M.; Zhao, Z.; Cheng, T.; Fortunelli, A.; Chen, C.-Y.; Yu, R.; Zhang, Q.; Gu, L.; Merinov, B. V.; Lin, Z.; Zhu, E.; Yu, T.; Jia, Q.; Guo, J.; Zhang, L.; Goddard, W. A., III; Huang, Y.; Duan, X. Ultrafine Jagged Platinum Nanowires Enable Ultrahigh Mass Activity for the Oxygen Reduction Reaction. *Science* **2016**, *354*, 1414−1419.

(11) Huang, X.; Zhao, Z.; Cao, L.; Chen, Y.; Zhu, E.; Lin, Z.; Li, M.; Yan, A.; Zettl, A.; Wang, Y. M.; Duan, X.; Mueller, T.; Huang, Y. High-Performance Transition Metal-Doped Pt₃Ni Octahedra for Oxygen Reduction Reaction. *Science* **2015**, *348*, 1230−1234.

(12) Stamenkovic, V. R.; Fowler, B.; Mun, B. S.; Wang, G.; Ross, P. N.; Lucas, C. A.; Marković, N. M. Improved Oxygen Reduction Activity on Pt3Ni(111) *via* Increased Surface Site Availability. *Science* **2007**, *315*, 493−497.

(13) Cui, C.; Gan, L.; Li, H.-H.; Yu, S.-H.; Heggen, M.; Strasser, P. Octahedral PtNi Nanoparticle Catalysts: Exceptional Oxygen Reduction Activity by Tuning the Alloy Particle Surface Composition. *Nano Lett.* **2012**, *12*, 5885−5889.

(14) Choi, S.-I.; Xie, S.; Shao, M.; Odell, J. H.; Lu, N.; Peng, H.-C.; Protsailo, L.; Guerrero, S.; Park, J.; Xia, X.; Wang, J.; Kim, M. J.; Xia, Y. Synthesis and Characterization of 9 nm Pt−Ni Octahedra with a Record High Activity of 3.3 A/mg_Pt for the Oxygen Reduction Reaction. *Nano Lett.* **2013**, *13*, 3420−3425.

(15) Bezerra, C. W. B.; Zhang, L.; Liu, H. S.; Lee, K. C.; Marques, A. L. B.; Marques, E. P.; Wang, H. J.; Zhang, J. J. A Review of Heat-Treatment Effects on Activity and Stability of PEM Fuel Cell Catalysts for Oxygen Reduction Reaction. *J. Power Sources* **2007**, *173*, 891−908.

(16) Cui, C.; Ahmadi, M.; Behafarid, F.; Gan, L.; Neumann, M.; Heggen, M.; Cuenya, B. R.; Strasser, P. Shape-Selected Bimetallic Nanoparticle Electrocatalysts: Evolution of Their Atomic-Scale Structure, Chemical Composition, and Electrochemical Reactivity under Various Chemical Environments. *Faraday Discuss.* **2013**, *162*, 91−112.

(17) Durst, J.; Lopez-Haro, M.; Dubau, L.; Chatenet, M.; Soldo-Olivier, Y.; Guétaz, L.; Bayle-Guillemaud, P.; Maillard, F. Reversibility of Pt-Skin and Pt-Skeleton Nanostructures in Acidic Media. *J. Phys. Chem. Lett.* **2014**, *5*, 434−439.

(18) Gasteiger, H. A.; Kocha, S. S.; Sompalli, B.; Wagner, F. T. Activity Benchmarks and Requirements for Pt, Pt-Alloy, and Non-Pt Oxygen Reduction Catalysts for PEMFCs. *Appl. Catal., B* **2005**, *56*, 9−35.

(19) Chi, M.; Wang, C.; Lei, Y.; Wang, G.; Li, D.; More, K. L.; Lupini, A.; Allard, L. F.; Markovic, N. M.; Stamenkovic, V. R. Surface Faceting and Elemental Diffusion Behaviour at Atomic Scale for Alloy Nanoparticles during *in Situ* Annealing. *Nat. Commun.* **2015**, *6*, 8925.

(20) Gan, L.; Heggen, M.; Cui, C.; Strasser, P. Thermal Facet Healing of Concave Octahedral Pt−Ni Nanoparticles Imaged *in Situ* at the Atomic Scale: Implications for the Rational Synthesis of Durable High-Performance ORR Electrocatalysts. *ACS Catal.* **2016**, *6*, 692−695.

(21) Beermann, V.; Gocyla, M.; Kühl, S.; Padgett, E.; Schmies, H.; Goerlin, M.; Erini, N.; Shviro, M.; Heggen, M.; Dunin-Borkowski, R. E.; Muller, D. A.; Strasser, P. Tuning the Electrocatalytic Oxygen Reduction Reaction Activity and Stability of Shape-Controlled Pt−Ni Nanoparticles by Thermal Annealing − Elucidating the Surface Atomic Structural and Compositional Changes. *J. Am. Chem. Soc.* **2017**, *139*, 16536−16547.

(22) Dai, S.; You, Y.; Zhang, S.; Cai, W.; Xu, M.; Xie, L.; Wu, R.; Graham, G. W.; Pan, X. *In Situ* Atomic-Scale Observation of Oxygen-Driven Core-shell Formation in Pt₃Co Nanoparticles. *Nat. Commun.* **2017**, *8*, 204.

(23) van der Vliet, D. F.; Wang, C.; Li, D. G.; Paulikas, A. P.; Greeley, J.; Rankin, R. B.; Strmcnik, D.; Tripkovic, D.; Markovic, N. M.; Stamenkovic, V. R. Unique Electrochemical Adsorption Properties of Pt-Skin Surfaces. *Angew. Chem., Int. Ed.* **2012**, *51*, 3139−3142.

(24) Han, B.; Carlton, C. E.; Kongkanand, A.; Kukreja, R. S.; Theobald, B. R.; Gan, L.; O'Malley, R.; Strasser, P.; Wagner, F. T.; Shao-Horn, Y. Record Activity and Stability of Dealloyed Bimetallic Catalysts for Proton Exchange Membrane Fuel Cells. *Energy Environ. Sci.* **2015**, *8*, 258−266.

(25) Arán-Ais, R. M.; Solla-Gullón, J.; Gocyla, M.; Heggen, M.; Dunin-Borkowski, R. E.; Strasser, P.; Herrero, E.; Feliu, J. M. The Effect of Interfacial pH on the Surface Atomic Elemental Distribution and on the Catalytic Reactivity of Shape-Selected Bimetallic Nanoparticles towards Oxygen Reduction. *Nano Energy* **2016**, *27*, 390−401.

(26) Strasser, P.; Kühl, S. Dealloyed Pt-Based Core-Shell Oxygen Reduction Electrocatalysts. *Nano Energy* **2016**, *29*, 166−177.

(27) Chen, C.; Kang, Y. J.; Huo, Z. Y.; Zhu, Z. W.; Huang, W. Y.; Xin, H. L. L.; Snyder, J. D.; Li, D. G.; Herron, J. A.; Mavrikakis, M.; Chi, M. F.; More, K. L.; Li, Y. D.; Markovic, N. M.; Somorjai, G. A.; Yang, P. D.; Stamenkovic, V. R. Highly Crystalline Multimetallic Nanoframes with Three-Dimensional Electrocatalytic Surfaces. *Science* **2014**, *343*, 1339−1343.

(28) Niu, Z.; Becknell, N.; Yu, Y.; Kim, D.; Chen, C.; Kornienko, N.; Somorjai, G. A.; Yang, P. Anisotropic Phase Segregation and Migration of Pt in Nanocrystals en Route to Nanoframe Catalysts. *Nat. Mater.* **2016**, *15*, 1188−1194.

(29) Becknell, N.; Son, Y.; Kim, D.; Li, D.; Yu, Y.; Niu, Z.; Lei, T.; Sneed, B. T.; More, K. L.; Markovic, N. M.; Stamenkovic, V. R.; Yang, P. Control of Architecture in Rhombic Dodecahedral Pt-Ni Nanoframe Electrocatalysts. *J. Am. Chem. Soc.* **2017**, *139*, 11678−11681.

(30) Gan, L.; Heggen, M.; Rudi, S.; Strasser, P. Core−Shell Compositional Fine Structures of Dealloyed Pt_xNi₁₋ₓ Nanoparticles and Their Impact on Oxygen Reduction Catalysis. *Nano Lett.* **2012**, *12*, 5423−5430.

(31) Becknell, N.; Kang, Y.; Chen, C.; Resasco, J.; Kornienko, N.; Guo, J.; Markovic, N. M.; Somorjai, G. A.; Stamenkovic, V. R.; Yang, P. Atomic Structure of Pt₃Ni Nanoframe Electrocatalysts by *in Situ* X-Ray Absorption Spectroscopy. *J. Am. Chem. Soc.* **2015**, *137*, 15817−15824.

(32) Toda, T.; Igarashi, H.; Uchida, H.; Watanabe, M. Enhancement of the Electroreduction of Oxygen on Pt Alloys with Fe, Ni, and Co. *J. Electrochem. Soc.* **1999**, *146*, 3750−3756.

(33) Li, Y.; Hart, J. L.; Taheri, M. L.; Snyder, J. D. Morphological Instability in Topologically Complex, Three-Dimensional Electrocatalytic Nanostructures. *ACS Catal.* **2017**, *7*, 7995−8005.

(34) Wan, L.-J.; Moriyama, T.; Ito, M.; Uchida, H.; Watanabe, M. *In Situ* STM Imaging of Surface Dissolution and Rearrangement of a Pt−Fe Alloy Electrocatalyst in Electrolyte Solution. *Chem. Commun.* **2002**, 58−59.

(35) Stephens, I. E.; Bondarenko, A. S.; Grønbjerg, U.; Rossmeisl, J.; Chorkendorff, I. Understanding the Electrocatalysis of Oxygen Reduction on Platinum and its Alloys. *Energy Environ. Sci.* **2012**, *5*, 6744−6762.

(36) Meier, J. C.; Galeano, C.; Katsounaros, I.; Witte, J.; Bongard, H. J.; Topalov, A. A.; Baldizzone, C.; Mezzavilla, S.; Schüth, F.; Mayrhofer, K. J. Design Criteria for Stable Pt/C Fuel Cell Catalysts. *Beilstein J. Nanotechnol.* **2014**, *5*, 44−67.